Zhang *et al. Journal of Ovarian Research* (2026) 19:110
https://doi.org/10.1186/s13048-026-02024-x

Journal of Ovarian Research

RESEARCH Open Access

Single-cell dissection of regulated cell death dynamics in ovarian aging

Qianyu Zhang[1,2,3], Yuanqu Zhao[1,2,3], Tong Wu[1,2,3], Gang Chen[1,2,3], Shixuan Wang[1,2,3], Mo Li[1,2,3*] and Jinjin Zhang[1,2,3*]

Abstract

Background Ovarian aging drives declining fertility, premature menopause, and systemic age-related diseases. Multiple different types of regulated cell death (RCD) pathways have been identified and play integral roles in diverse physiological and pathological processes. However, the RCD landscape of ovarian aging remains uncharacterized at single-cell resolution.

Results Here, we conducted single-cell RNA sequencing (scRNA-seq) on murine ovaries across aging (3, 9, 12 and 15 months), and mapped pan-RCD dynamics, including apoptosis, ferroptosis, parthanatos, and ten other pathways, revealing cell-type-specific RCD trajectories. These pathways exhibited distinct changes with ovarian aging, highlighting cell heterogeneity. Notably, apoptosis and parthanatos pathways demonstrated high correlations and rates of change with advancing age. Parthanatos was particularly notable for exhibiting one of the steepest age-associated increases. Cross-species validation using human ovarian scRNA-seq and GTEx V8 transcriptomics confirmed conserved parthanatos upregulation with age, negatively correlating with the expression levels of key enzymes in hormone synthesis.

Conclusions The study deciphers the RCD patterns in murine and human ovarian aging, nominating parthanatos as a targetable node for combating ovarian aging and enhancing female fertility.

Keywords Aging, Ovary, Gene expression profiling, Regulated cell death, Single-cell RNA sequencing, Parthanatos.

Background

The ovary is a crucial organ for females due to its indispensable functions in oogenesis and sex hormone secretion [1], yet it undergoes accelerated aging characterized by irreversible follicular depletion [2]. In contemporary society, the trend towards delayed childbearing and the subsequent challenges in achieving successful pregnancies have heightened the focus on addressing ovarian aging [3]. Critically, ovarian aging extends beyond fertility loss, correlating with systemic aging acceleration [4], increased risk of cardiovascular disease [5], cancer [6], cognitive decline [7], and all-cause mortality [8]. Elucidating the molecular drivers of ovarian aging is thus imperative for developing protective interventions.

*Correspondence:
Mo Li
limo_Rachel@163.com
Jinjin Zhang
jinjinzhang@tjh.tjmu.edu.cn
[1]Department of Obstetrics and Gynecology, Tongji Hospital, Tongji Medical College, Huazhong University of Science and Technology, Wuhan, Hubei 430030, China
[2]National Clinical Research Center for Obstetrical and Gynecological Diseases, Wuhan, Hubei 430030, China
[3]Key Laboratory of Cancer Invasion and Metastasis, Ministry of Education, Wuhan, Hubei 430030, China

Regulated cell death (RCD), distinct from accidental cell death (ACD), is characterized by tightly orchestrated signaling cascades and molecularly defined effector mechanisms [9]. Beyond its established roles in organogenesis [10, 11] and tissue homeostasis [12, 13], RCD modulates stress responses [14] and aging pathologies. While apoptosis was the first identified form of RCD, recent work implicates diverse non-apoptotic RCD modalities. These include, but are not limited to, autophagy-dependent cell death, cuproptosis, disulfidptosis, entotic cell death, ferroptosis, lysosome-dependent cell death, necroptosis, netotic cell death, oxeiptosis, parthanatos, PANoptosis and pyroptosis [9, 15–17]. These pathways exhibit crosstalk through shared regulators [18], forming an integrated RCD network. Recent findings underscore the involvement of diverse RCD pathways [19] in the process of ovarian aging, beyond the recognized apoptosis [20]. For instance, the increased follicle numbers observed in Nlrp3$^{-/-}$ aging mice suggested a potential role for pyroptosis [21]. Additionally, elevated levels of poly ADP-ribose (PAR) expression and the nuclear translocation of apoptosis-inducing factor (AIF) in cumulus granulosa cells (GCs) of patients with diminished ovarian reserve (DOR) implied the involvement of the PARP1-dependent cell death pathway [22]. In non-human primates, ovarian aging is characterized by an increase in apoptosis in aged GCs [23]. In aged human ovaries, there was a notable activation of the pyroptosis pathway within macrophages [24]. Recently, some strategies have been demonstrated to work by targeting RCD. For example, quercetin and melatonin have exhibited ovarian protection properties by regulating autophagy in granulosa cells [25, 26], while spermidine alleviated ovarian damage by suppressing ferroptosis [27]. Despite these findings, cell-type-specific RCD dynamics across ovarian compartments remain uncharacterized, and the relative contributions of distinct RCD pathways to aging phenotypes lack systematic evaluation.

Here, we constructed a single-cell transcriptomics of murine ovaries across aging trajectories and integrated these findings with cross-species datasets to: (1) map cell-type-resolved dynamics of RCD pathways, including apoptosis, ferroptosis, parthanatos, etc.; (2) prioritize RCD pathways that show strong age-associated changes across ovarian cell types; and (3) develop RCD-based predictive tools for ovarian aging. Together, this work provides a single-cell resource and a comparative framework for studying conserved, age-associated RCD signatures in ovarian aging, and it motivates future mechanistic and interventional studies.

Methods

Estrous cycle monitoring and confirmation

Vaginal fluid was collected by vaginal lavage at 10:00 AM each morning using a pipette containing 20 μL sterile saline, which was gently introduced into the vaginal canal and then withdrawn. The recovered fluid was evenly smeared onto glass slides and air-dried. Slides were then stained with hematoxylin and eosin (H&E; hematoxylin for 5 min followed by eosin for 2 min) and examined under a light microscope [28]. Estrous stages were classified based on vaginal cytology as proestrus, estrus, metestrus, or diestrus. Proestrus showed a predominance of nucleated epithelial cells with prominent hematoxylin-positive nuclei. Estrus was characterized by large numbers of cornified epithelial cells that were typically anucleate and showed eosinophilic cytoplasm, with few leukocytes. Metestrus displayed a mixed cell population with cornified epithelial cells accompanied by an increase in leukocytes [29]. Diestrus was defined by a predominance of leukocytes with only limited epithelial cells. Diestrus on the day of euthanasia was confirmed by the above cytological features.

Murine ovary dissociation and single-cell isolation

The female C57BL/6 mice were supplied by Beijing Vital River Laboratory Animal Technology Co., Ltd. These mice were kept under a 12 h light/12 h dark cycle with no water or food restriction. The mice were humanely euthanized at the diestrus stage. A combination of carbon dioxide anesthesia and cervical dislocation was employed to ensure a rapid and painless procedure that strictly adhered to humane endpoint principles, thereby minimizing animal anxiety and discomfort. Fresh ovaries were then obtained from C57BL/6 mice aged 3-month-old (OVA3M), 9-month-old (OVA9M), 12-month-old (OVA12M), and 15-month-old (OVA15M). Body weight and ovary weight were recorded. Only one side of the ovaries from each sample was used for scRNA-seq. Due to the size of mouse ovaries, six ovaries from the same age group were pooled [30]. Then the fresh tissues were stored in the sCelLiveTM Tissue Preservation Solution (Singleron) on ice, washed with Hanks Balanced Salt Solution (HBSS) 3 times, and then digested with 3 ml sCelLiveTM Tissue Dissociation Solution (Singleron) by Singleron PythoN™ Automated Tissue Dissociation System (Singleron) at 37 °C for 15 min. Afterward, for the removal of red blood cells, the GEXSCOPE® red blood cell lysis buffer (Singleron, 2 ml) was added, and cells were incubated at 25 °C for another 10 min. The solution was then centrifuged at 300 g, 4 °C for 5 min to remove the supernatant and suspended softly with PBS. Finally, the samples were stained with trypan blue (Sigma, United States) and the cellular viability was evaluated microscopically.

Single-cell library construction and sequencing

Single-cell suspensions (1 × 105 cells/mL) with PBS (HyClone) were loaded onto a microwell chip using the Singleron Matrix® Single Cell Processing System. Barcoding Beads are subsequently collected from the microwell chip, followed by reverse transcription of the mRNA captured by the Barcoding Beads to obtain cDNA, and PCR amplification. The amplified cDNA is then fragmented and ligated with sequencing adapters. The scRNA-seq libraries were constructed according to the protocol of the GEXSCOPE® Single Cell RNA Library Kits (Singleron) [31]. After quality checks, individual libraries were diluted to 4 nM, pooled, and sequenced on Illumina Novaseq 6000 with 150 bp paired-end reads.

Clustering, cell type identification and annotation

The R package 'Seurat' (http://satijalab.org/seurat/, Version 4.4.0) was used for quality control, dimensionality reduction and clustering. Firstly, cells that met the following criteria were aborted: (1) cells with a gene count less than 200 or with a top 2% gene count; (2) cells with a top 2% UMI count; (3) cells with mitochondrial content > 50%. Besides, genes expressed in fewer than 5 cells were excluded. After filtering, 30,234 ovarian cells (8064 from the OVA3M, 7498 from the OVA9M, 7055 from the OVA12M and 7617 from the OVA15M) were retained for the downstream analyses, with an average of 2206 genes per cell, and 7093 UMIs per cell. Then, the 'NormalizeData' function was applied to normalize the gene expression (UMI counts), and the 'ScaleData' function was used to center the expression data for dimensional reduction analysis. The top 2000 variable genes were identified using the 'FindVariableFeatures' function for PCA analysis. Cells were then separated into 37 clusters with the 'FindClusters' function at resolutions of 1.8 (OVA) based on the top 20 principal components. The batch effect between samples was removed by Harmony [32], which iteratively removed batch effects in the PCA space. Finally, the visualization of cell clusters was achieved using t-Distributed Stochastic Neighbor Embedding (t-SNE) or Uniform Manifold Approximation and Projection (UMAP) with Seurat functions 'RunTSNE' and 'RunUMAP'.

To annotate each cell cluster, we first screened DEGs between the cluster and the rest clusters by 'FindAllMarkers'. Afterward, the cell type of each cluster was determined with the expression of canonical markers found in the DEGs using the SynEcoSys database. The annotation of the subtypes of immune cells was determined according to the 'ImmGenData'/ 'MouseRNAseqData' annotation library of SingleR (Version 2.4.0).

Public dataset acquisition

We collected the mouse and human ovarian RNA datasets of different ages [33] in the Gene Expression Omnibus (GEO) database (https://www.ncbi.nlm.nih.gov/geo/) and the GTEx V8 dataset. GSE154890 [34] contained bulk RNA-seq data of murine ovary samples from 3-month-old (n = 5), 6-month-old (n = 5), 9-month-old (n = 5), and 12-month-old (n = 5) mice. GSE202601 contained single-nucleus RNA sequence data of 4 young and 4 reproductively aged human ovaries. The raw expression data of both datasets and their GPL platform files were downloaded, and the expression matrix was annotated using gene symbols. RNA-seq data of human ovaries were obtained from the GTEx V8 dataset. Clinical information for the samples is in the Supplementary Table 5. For subsequent analysis, 22 samples from the 20–29 age group and 61 samples from the 50–59 age group were selected after screening.

Differentially expressed genes (DEGs) analysis

For the RNA-seq data, 'DESeq2' (Version 1.40.2) [35] was used to analyze differentially expressed genes ($|Log_2FC| > 1$ and adjusted P-value < 0.05) among groups. While for the scRNA-seq/snRNA-seq data, differential expression analysis for each cell type was performed using the Wilcoxon likelihood ratio test of the 'FindMarkers' function of the 'Seurat' package with default parameters ($|Log_2FC| > 0.25$, adjusted P-value < 0.05).

Gene enrichment analysis

The functional enrichment analysis of Gene Ontology (GO) and Kyoto Encyclopedia of Genes and Genomes (KEGG) was performed with the R package 'clusterProfiler' (Version 4.8.3) [36]. GO/KEGG terms or pathways with an adjusted P-value less than 0.05 were considered as significantly enriched functions. The enrichment results of SuperPath were obtained from GeneAnalytics (https://geneanalytics.genecards.org/). Gene set enrichment analysis (GSEA) was also performed to identify the underlying pathways during ovarian aging using 'clusterProfiler', with the threshold for significant terms being adjusted P-value < 0.05. Graphics of bar charts or dot plots of gene enrichment analysis were generated with the R package 'ggplot2' (https://github.com/tidyverse/ggplot2).

Scoring of pathway activity

We collected the key genes of 13 RCD pathways from various sources, including the Kyoto Encyclopedia of Genes and Genomes (KEGG) Database, the Molecular Signatures Database, the Reactome Database, and review articles [37]. The final gene lists of 13 different kinds of RCD are shown in Supplementary Table 6. The following types of cell death pathways were included: apoptosis

(136 genes for human and 161 genes for mouse), autophagy-dependent cell death (165 genes for human and 249 genes for mouse), cuproptosis (14 genes for human and mouse), disulfidptosis (3 genes for human and 4 for mouse), entotic cell death (14 genes for human and 17 genes for mouse), ferroptosis (41 genes for human and 89 genes for mouse), lysosome-dependent cell death (210 genes for human and 214 genes for mouse), necroptosis (159 genes for human and 100 genes for mouse), netotic cell death (7 genes for human and mouse), oxeiptosis (5 genes for human and mouse), parthanatos (9 genes for human and mouse), pyroptosis (37 genes for human and 32 genes for mouse), PANoptosis (19 genes for human and mouse). In total, 920 mouse genes and 819 human genes related to RCD were collected.

For the RNA-seq data, single sample gene set enrichment analysis (ssGSEA) was used in the Gene Set Variation Analysis (GSVA) package (Version 1.48.3) [38] to calculate the scores of 13 types of regulated cell death pathways in each sample and the differences between different groups were detected using the 'limma' package (Version 3.56.2) [39]. To perform pathway activity analysis on scRNA-seq/snRNA-seq generated cell clusters, the "UCell" package (Version 2.4.0) [40] was utilized to calculate the UCell scores of each cell, which was based on the Mann-Whitney U statistic by ranking query genes in the order of their expression levels in individual cells. The comparisons of changes of UCell scores in different ages and clusters were visualized by the R package 'ggpubr' (Version 0.6.0) (https://rpkgs.datanovia.com/ggpubr/).

Age slope of UCell score

To quantify the UCell score of each pathway increase over time (aging velocity), a linear model was established with the design: UCell score ~ age + RCD pathway + age: RCD pathway (score explained by a two-factor model including interaction term) using the linear model function in R. We used the "lstrends" function from the "lsmeans" package [41], which utilizes least-square means to estimate and compare the slopes of fitted lines for each region.

Weighted gene correlation network analysis (WGCNA)

WGCNA was performed using the "WGCNA" package (version 1.72) in R [42]. We selected the top 8,000 genes with the highest median absolute deviation (MAD) to construct the representation matrix, and a soft-threshold power of 11 was set using the "pickSoftThreshold" function. We used hierarchical clustering to identify modules of highly interconnected genes based on their connectivity and covariance coefficients. A heatmap was plotted to reflect the relationships between each module and the RCD pathways. The modules were constructed with a module dendrogram threshold of 0.25 and a minimum module size of 30 genes.

Lasso regression

The Least Absolute Shrinkage and Selection Operator (LASSO) was used to construct the parthanatos risk score [43]. The risk score formula was as follows: $= \sum_{i=1}^{n} \beta\, i * \exp(i)$. The $\exp(i)$represented the gene expression value, and $\beta\, i$ represented the LASSO coefficient. In this way, each sample can be calculated with a parthanatos score through the formula.

Human samples

A total of 14 women aged 20–29 ($n = 5$) and ≥ 50 years ($n = 9$) with ovaries were screened and selected by the Department of Pathology of Tongji Hospital. These patients had diagnoses of conditions including cervical intraepithelial neoplasia III or FIGO stage I cervical cancer along with ovarian cysts and FIGO stage I ovarian malignancies. All patients had definite clinical and pathological diagnoses that necessitated surgical intervention, and there were no identified contraindications to surgery. All patients signed informed consent and it was ascertained that they had no fertility requirements. The surgical methods adhered to the pertinent guidelines and consensus statements. All pathological sections were independently examined by two pathologists to confirm the absence of cancer cells. Paraffin-embedded sections of the ovaries from patients, which exhibited relatively normal histological features, were harvested for subsequent hematoxylin and eosin (H&E) staining.

Hematoxylin and Eosin (H&E) staining

H&E staining was performed as previously described [23]. Ovaries were preserved in 4% PFA and sectioned at a 5-μm thickness. Next, the tissue slides were treated with xylene and then rehydrated using a graded series of ethanol (100%, 100%, 95%, 80%, 75%). The slides were briefly washed in distilled water and then incubated with a hematoxylin solution. The sections were then washed with running tap water to remove excess hematoxylin. Subsequently, the sections were differentiated in 1% acid alcohol for 30 s and washed again in running water for 1 min. The sections were then counterstained with eosin and dehydrated in a graded series of ethanol (75%, 80%, 95%, 100%, 100%) and 100% xylene.

Hormone measurements

Enzyme-linked immunosorbent assay following the kit instructions (Cusabio Technology LLC, USA) was performed to detect the concentrations of AMH and E2 in the serum samples.

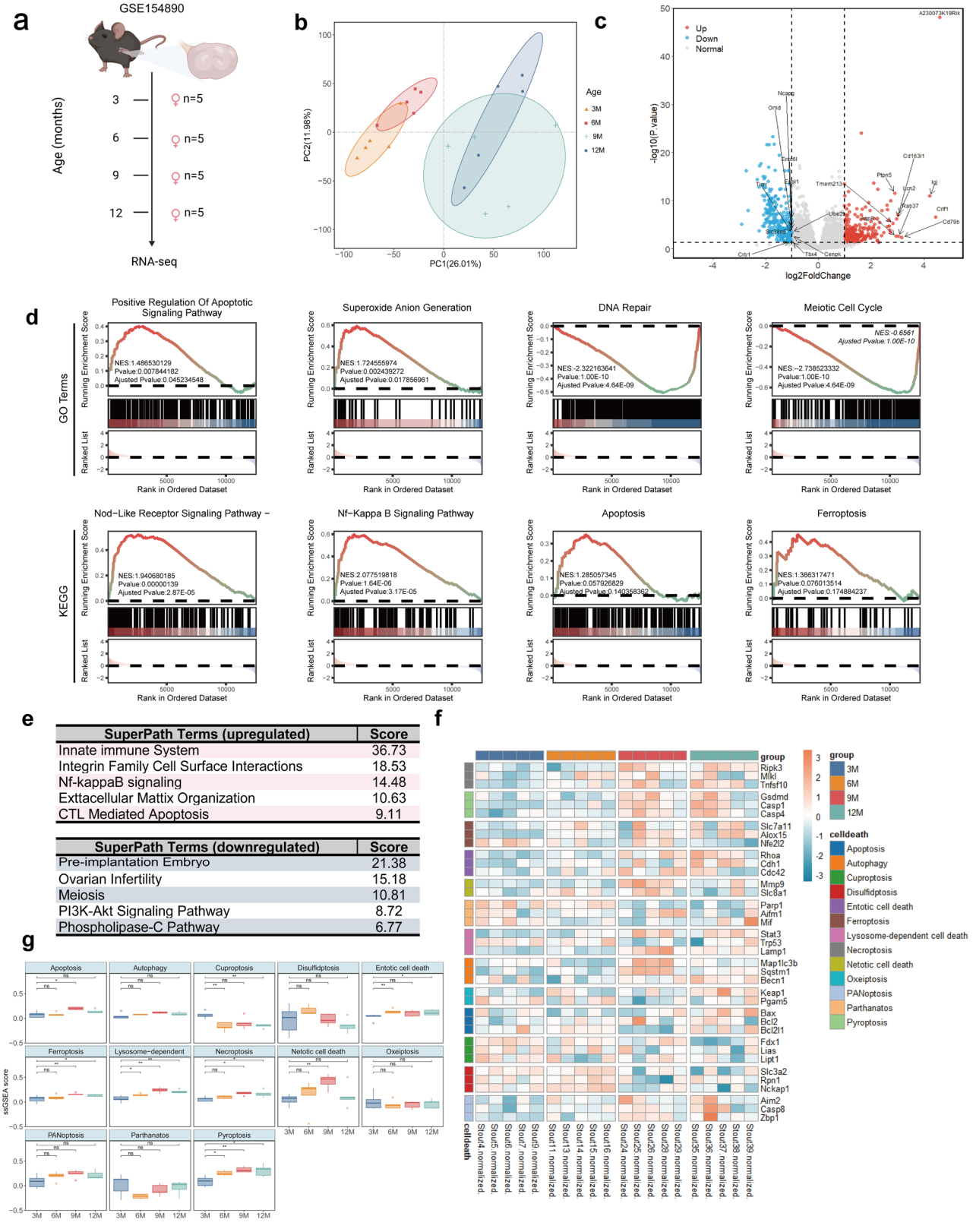

SuperPath Terms (upregulated)	Score
Innate immune System	36.73
Integrin Family Cell Surface Interactions	18.53
Nf-kappaB signaling	14.48
Exttacellular Mattix Organization	10.63
CTL Mediated Apoptosis	9.11

SuperPath Terms (downregulated)	Score
Pre-implantation Embryo	21.38
Ovarian Infertility	15.18
Meiosis	10.81
PI3K-Akt Signaling Pathway	8.72
Phospholipase-C Pathway	6.77

Fig. 1 (See legend on next page.)

(See figure on previous page.)

Fig. 1 Function and pathway enrichment analysis using data online indicated a role of regulated cell death (RCD) in murine ovarian aging. **a** Cohort overview. Ovaries were collected from female 3-month-age (OVA3M, $n=5$), 6-month-age (OVA6M, $n=5$), 9-month-age (OVA9M, $n=5$) and 12-month-age (OVA12M, $n=4$) C57BL/6 mice in the GSE154890 dataset. **b** Sample correlation via PCA plot. **c** Volcano plot showing 568 significantly differentially expressed genes (DEGs, $|\log_2 FC| > 0.25$, adjusted $P < 0.05$) between OVA3M and OVA12M groups. The upregulated or downregulated genes that exhibited the highest 10 $\log_2 FC$ are labeled. **d** Gene Set Enrichment Analysis (GSEA) based on the GO dataset and KEGG databases. **e** SuperPath enrichment analysis of the DEGs between OVA3M and OVA12M groups. **f** Heatmap of the expression of key RCD-related genes in each age group. **g** ssGSEA analysis of 13 RCD pathways demonstrated by boxplots in each age group. ns, not significant; * $P < 0.05$; ** $P < 0.01$; P values by one-way ANOVA test

Immunohistochemistry

Paraffin-embedded ovaries were cut into 4 μm sections and baked at 65℃ for 60 min. The sections were deparaffinized with xylenes and rehydrated. Antigen retrieval was performed by microwaving sections in EDTA buffer. Endogenous peroxidase activity was quenched with 3% H_2O_2, followed by blocking with 5% BSA. Then sections were incubated with anti-8-OHdG primary antibody (ab62623, Abcam, 1:200) overnight at 4℃. After washing, a biotinylated anti-rabbit secondary antibody (Boster Biological Technology, Wuhan, China) was applied, and signals were visualized using DAB (Servicebio, Wuhan, China).

Immunofluorescence

Ovarian paraffin Sect. (4 μm) were baked at 65 °C for 60 min, deparaffinized in xylene, and rehydrated. Sections were then submerged in EDTA antigenic retrieval buffer and microwaved for antigenic retrieval, followed by blocking with 5% BSA. Sections were then incubated overnight at 4 °C with primary antibodies. After washing, sections were incubated with fluorescent-dye-conjugated secondary antibodies. Nuclei were counterstained with DAPI (Servicebio, Wuhan, China). Primary antibodies included anti-AIF (A2568, ABclonal, 1:200), anti-PAR (D9P7Z, Cell Signaling Technology, 1:200), anti-γ-H2AX (BLR053F, ThermoFisher, 1:200).

Western blot analysis

Western blot analysis was performed to measure protein expression levels. Ovaries were lysed in RIPA lysis buffer (Servicebio, Wuhan, China), followed by centrifugation to isolate the supernatant. Protein samples were resolved by 10% SDS-PAGE and transferred onto a PVDF membrane (Cytiva, Shanghai, China). The membrane was blocked with 5% non-fat milk for 2 h at room temperature, then incubated overnight with primary antibodies, including anti-AIF (ABclonal, 1:1000), anti-PAR (D9P7Z, Cell Signaling Technology, 1:1000), anti-PARP (46D11, Cell Signaling Technology, 1:1000), and anti-MIF (E8S8H, Cell Signaling Technology, 1:1000) at 4 °C. After washing, secondary antibodies were applied for 1 h at room temperature. Protein signals were detected using ECL reagent (Thermo Fisher, Waltham, MA, USA), and band intensities were quantified with ImageJ software (NIH).

Statistical analysis

All statistical tests were implemented utilizing R version 4.3.2 (https://www.r-project.org/). The bar plots showed means ± SEM of the data. Statistical analyses were performed using two-tailed Student's t-test, One-way ANOVA, or Wilcoxon rank-sum tests. Correlation analysis between the variables was conducted using Pearson's correlation test. Statistical significance levels were set as P-value < 0.05 or adjusted P-value < 0.05, as clarified in the figure legends and main text. In all figures, one, two, and three asterisks indicate * $P < 0.05$, ** $P < 0.01$, *** $P < 0.001$, **** $P < 0.0001$, respectively. 'ns' indicates not significant.

Results

Public dataset reveals cell death-related pathways activation in murine ovarian aging

To preliminarily investigate the changing RCD characteristics in the murine ovarian microenvironment throughout the reproductive lifespan, we conducted an extensive search of the public datasets. The GSE154890 dataset contains RNA sequencing data of ovaries from mice of 3-month-old (OVA3M), 6-month-old (OVA6M), 9-month-old (OVA9M) and 12-month-old (OVA12M) (Fig. 1a). The PCA plot revealed greater similarities between OVA3M and OVA6M, as well as between OVA9M and OVA12M, indicating that murine ovarian aging may occur as early as 9-month-old (Fig. 1b). Therefore, to comprehend more aging signatures, we compared the differentially expressed genes (DEGs) between OVA12M and OVA3M (adjusted P-value < 0.05 and $|\log_2 FC| > 1$), identifying 304 upregulated genes and 264 downregulated genes (Fig. 1c). Subsequently, to investigate the potential pathways and mechanisms contributing to ovarian aging, we performed an enrichment analysis based on these DEGs using various databases. GSEA based on the GO and KEGG databases revealed age-associated pathway alterations. In GO, pathways related to apoptosis regulation and oxidative stress were significantly enriched, including positive regulation of apoptotic signaling pathway (NES = 1.4865, $P = 0.00784$, adjusted $P = 0.0452$) and superoxide anion generation (NES = 1.7246, $P = 0.00244$, adjusted $P = 0.0179$). In contrast, DNA repair (NES = − 2.4868, $P = 1.0 \times 10^{-10}$, adjusted $P = 4.64 \times 10^{-9}$) and meiotic cell cycle (NES = − 2.7385, $P = 1.0 \times 10^{-10}$, adjusted $P = 4.64 \times 10^{-9}$) were significantly depleted. In KEGG, inflammatory pathways such as the

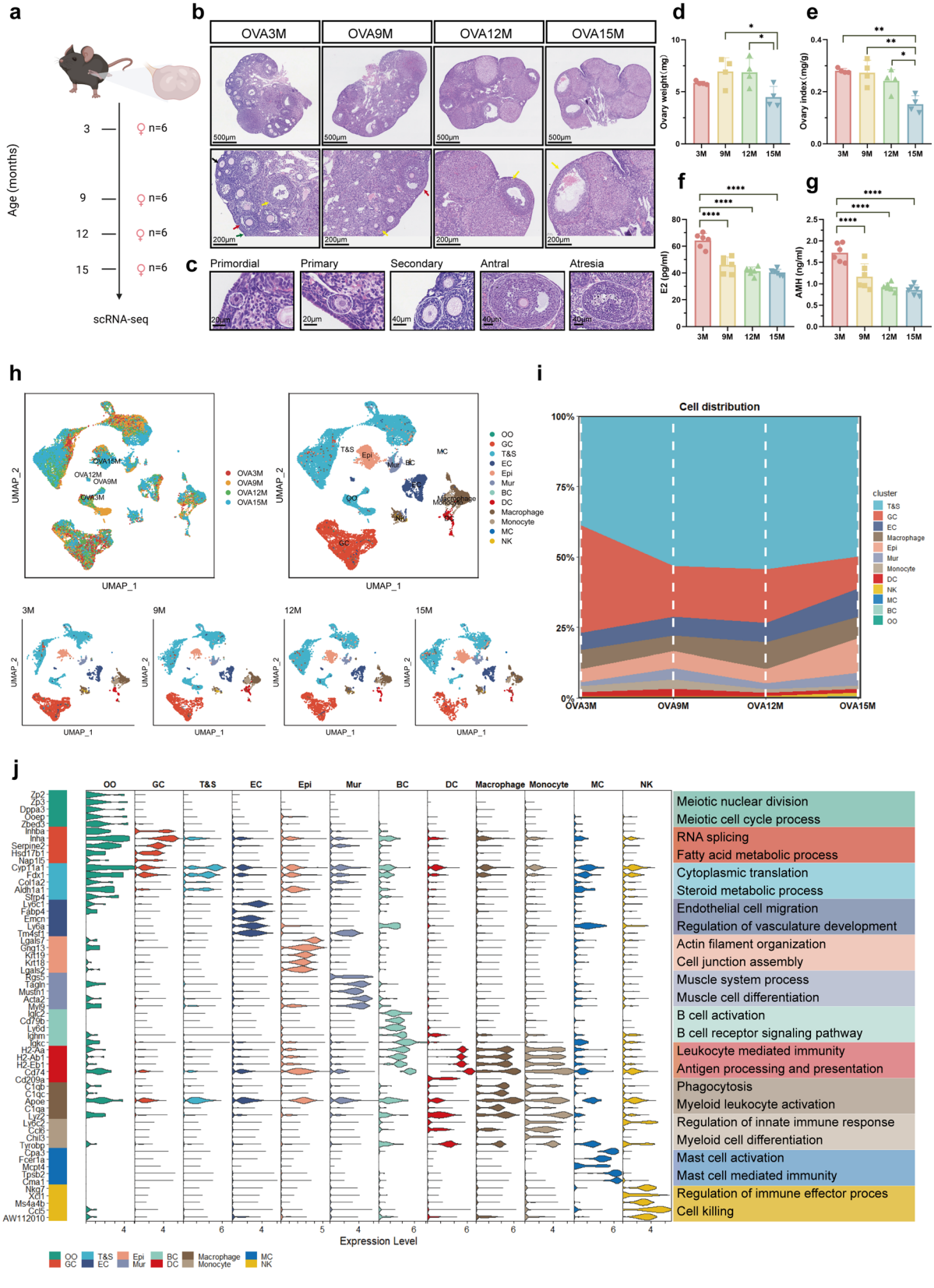

Fig. 2 (See legend on next page.)

(See figure on previous page.)

Fig. 2 A single-cell atlas of murine ovaries was constructed. **a** Cohort overview. Ovaries for scRNA sequencing were collected from female 3-month-age (OVA3M, $n=6$), 9-month-age (OVA9M, $n=6$), 12-month-age (OVA12M, $n=6$) and 15-month-age (OVA15M, $n=6$) C57BL/6 mice. **b** Hematoxylin and eosin (H&E) staining of the ovaries in each age group. Green, black, red and yellow arrowheads denote primordial follicles, primary follicles, antral follicles and atretic follicles, respectively. **c** Representative images (circled by the white dotted line) of follicles stained by H&E. **d-e** Changes in the ovary weight and ovary index with age. $n=4$ mice for each group. **f-g** Serum levels of E2 and AMH in female mice. $n=6$ mice for each group. **h** UMAP plots showing the cells in the ovaries that were captured by scRNA-seq and colored by age (left and bottom) and cell type (right). **i** Stacked bar chart showing the proportion of major cell types in each age group. **j**, Violin plot showing the top 5 marker gene expression levels for each cell type in the murine ovary (left). Representative GO terms for cell type-specific genes are shown (right). ns, not significant; * $P<0.05$; ** $P<0.01$; P values by one-way ANOVA test

NOD-like receptor signaling pathway (NES = 1.9407, $P=1.39\times10^{-6}$, adjusted $P=2.87\times10^{-5}$) and the NF-κB signaling pathway (NES = 2.0775, $P=1.64\times10^{-6}$, adjusted $P=3.17\times10^{-5}$) were significantly enriched. By contrast, KEGG Apoptosis (NES = 1.2851, FDR = 0.1404) and Ferroptosis (NES = 1.3663, FDR = 0.1749) showed positive enrichment scores but did not remain significant after multiple-testing correction and are therefore reported as enrichment trends (Fig. 1d). Similar results were observed in the SuperPath enrichment analysis, where immune-related, cell death-related, as well as ovarian microenvironment-related pathways were upregulated. In contrast, downregulated pathways were associated with declined ovarian function, such as "Pre-implantation embryo" and "Ovarian infertility", etc. (Fig. 1e). These findings indicate that dysregulation of several pathways is critical for maintaining ovarian function, especially cell death and inflammation.

Based on the findings, we conducted a systematic comparison of gene expression related to multiple RCD pathways across four distinct age groups. Our analysis revealed that genes associated with the majority of these pathways demonstrated increased expression levels in the older age groups (OVA9M and OVA12M) relative to the younger groups (OVA3M and OVA6M) (Fig. 1f). To further elucidate the response status of these RCD pathways at various developmental stages, we conducted single-sample Gene Set Enrichment Analysis (ssGSEA) to calculate the enrichment scores for 13 different RCD pathways and made comparisons between the OVA3M group and the other older groups. As shown in Fig. 1g, significant age-related changes in the activities of eight pathways were observed, including apoptosis, cuproptosis, entotic cell death, ferroptosis, lysosome-dependent cell death, necroptosis, netotic cell death, and pyroptosis. Collectively, these findings indicate that the activity of RCD pathways may have a substantial interaction with ovarian aging.

Construction of a single-cell transcriptome atlas of murine ovaries across the reproductive lifespan

To gain a deeper understanding of the cellular and molecular alterations associated with ovarian aging and to assess RCD pathways at single-cell resolution, we performed scRNA-seq on mouse ovaries at 3, 9, 12, and 15 months. Guided by the bulk RNA-seq overview in Fig. 1, where 6-month samples showed limited separation from 3-month samples in PCA (Fig. 1b), we prioritized sequencing resources toward 9 ~ 15 months to better capture aging associated transitions and to approximate a late reproductive transition context, as 15 months has been widely described as reproductively senescent in mice [44, 45] (Fig. 2a). Prior to conducting the aging research, we assessed the suitability of the age intervals by evaluating the changes in ovarian morphology. Consistent with previous findings, by 9 months of age, there was a significant reduction in the presence of visibly healthy follicles across all developmental stages, as shown in Fig. 2b and c. By the age of 15 months, healthy follicles were almost undetectable, having been largely supplanted by atretic follicles and corpora lutea. Additionally, the ovarian weight initially exhibited an increase followed by a subsequent decline over time. Correspondingly, the ovary index, defined as the ratio of ovarian weight to body weight, showed a significant reduction by 15 months of age (Fig. 2d and e). Serum estradiol (E2) (Fig. 2f) and AMH (Fig. 2g) decreased with age. This pattern suggests a decline in both the relative size and functional capacity of the ovaries with advancing aging.

After batch-effect correction and stringent cell filtration, 30,234 ovarian cells (8,064 from the OVA3M, 7,498 from the OVA9M, 7,055 from the OVA12M and 7,617 from the OVA15M) were retained. Unbiased clustering analysis identified 37 distinct cell clusters in the ovaries, and subsequently 12 major cell types were annotated based on their expression of type-specific and canonical marker genes: oocytes (OOs), granulosa cells (GCs), theca and stromal cells (T&Ss), epithelial cells (Epis), mural cells (Murs), endothelial cells (ECs), B cells (BCs), dendritic cells (DCs), macrophages, monocytes, mast cells (MCs), and natural killer cells (NKs) (Fig. 2h and Supplementary Table 1). Figure 2j shows scaled expression levels of the top five subtype-specific genes and representative GO terms in each cell type. Out of these 12 major cell types, OOs were captured in the OVA3M and OVA15M groups, while MCs were absent in the OVA9M group. The relative frequency of each cell type differed significantly. The proportion of T&Ss, ECs, Epis, Murs, macrophages, MCs and NKs generally increased with age. In contrast, the proportion of GCs, BCs, DCs, monocytes and OOs declined markedly. These alterations reflect age-related changes in cellular composition,

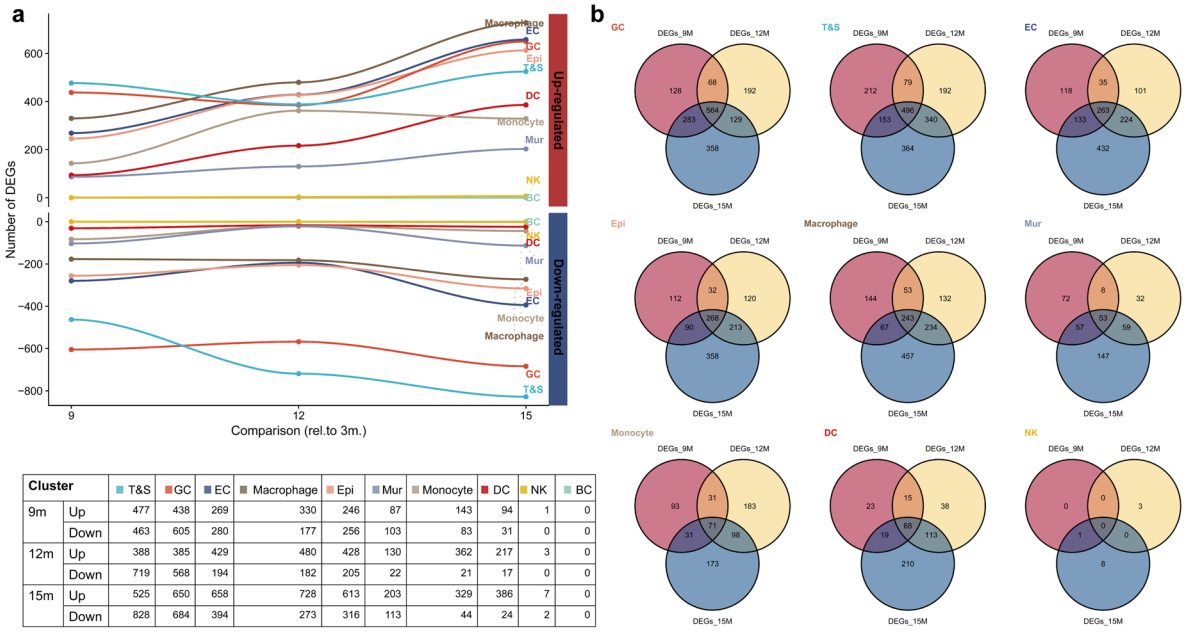

Cluster		T&S	GC	EC	Macrophage	Epi	Mur	Monocyte	DC	NK	BC
9m	Up	477	438	269	330	246	87	143	94	1	0
	Down	463	605	280	177	256	103	83	31	0	0
12m	Up	388	385	429	480	428	130	362	217	3	0
	Down	719	568	194	182	205	22	21	17	0	0
15m	Up	525	650	658	728	613	203	329	386	7	0
	Down	828	684	394	273	316	113	44	24	2	0

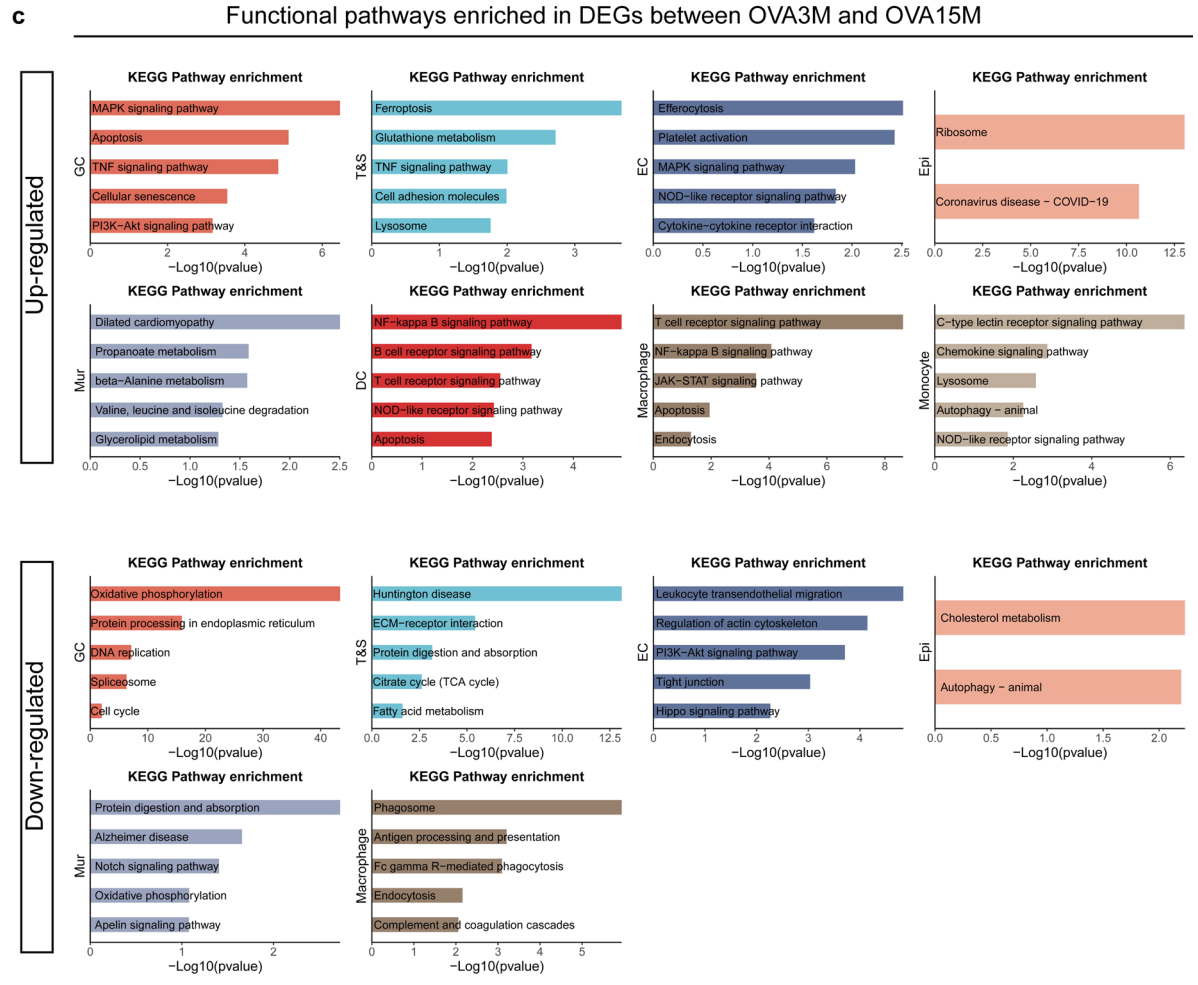

Fig. 3 Dynamic gene-expression patterns of the murine ovary at stepwise developmental stages. **a** Smoothed line plot displaying number of DEGs ($|\log_2 FC| > 0.25$, adjusted $P < 0.05$) for pairwise comparisons. Positive (negative) values represent up-regulated (down-regulated) genes (top). Table of data in the plot (bottom). **b** Venn plots showing the number of shared DEGs (compared to OVA3M) of each cell type between different groups. **c** Representative GO terms of age-related upregulated (top) and downregulated (bottom) of DEGs in different ovarian cell types

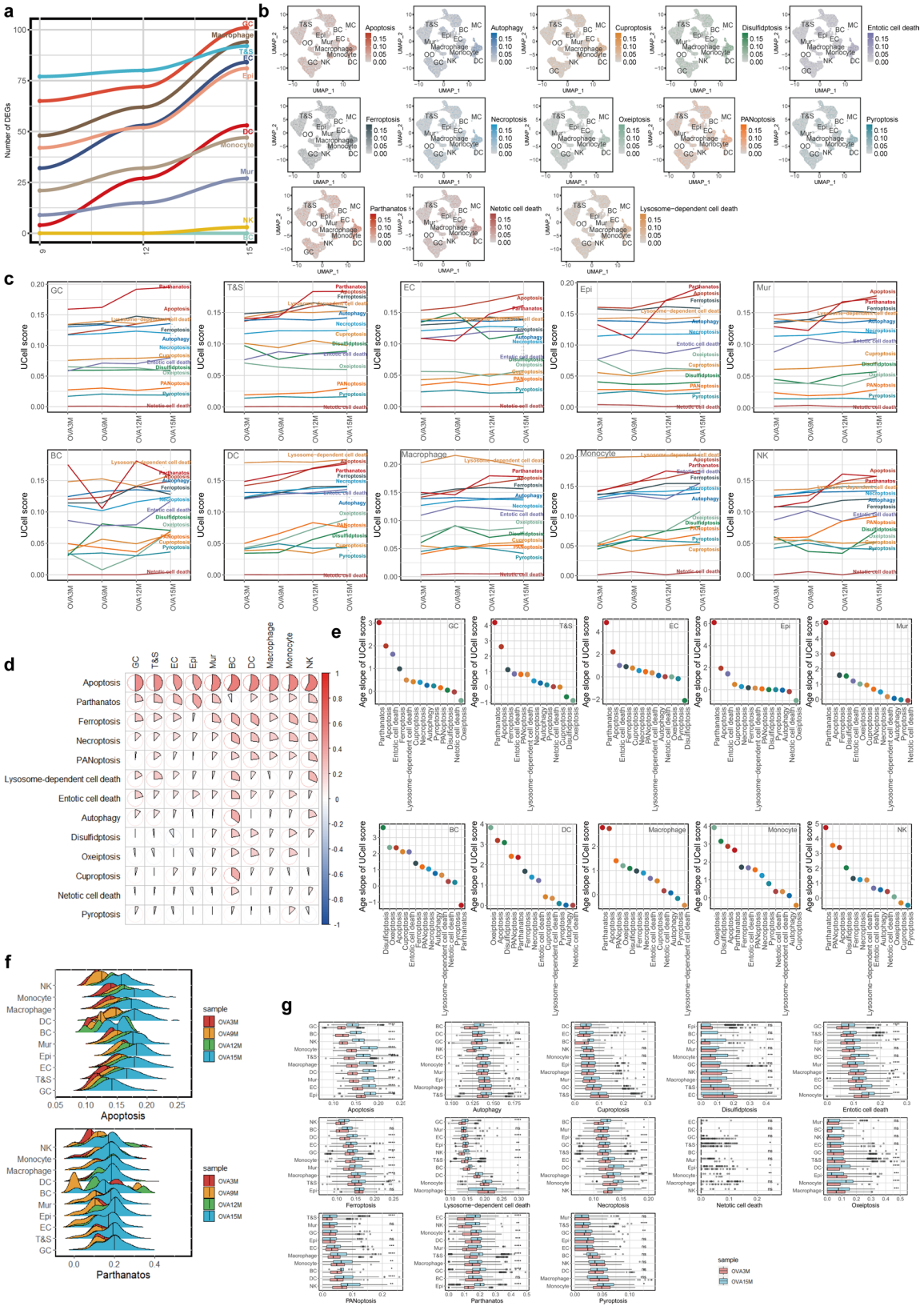

Fig. 4 (See legend on next page.)

(See figure on previous page.)

Fig. 4 RCD-related signatures changed during murine ovarian aging as revealed by scRNA sequencing. **a** Smoothed line plot displaying the number of RCD-related DEGs for pairwise comparisons. **b** Pathway activity across different cell types in the overall ovarian dataset, presented by a UMAP plot, with higher-scoring cells being brighter in color. **c** Smoothed line plot showing the changes of the UCell scores for each pathway across four age groups, colored by RCD pathway. **d** Pie plot showing the correlation between the UCell scores of pathways and chronological age in each cell type. **e** Slope of linear regressions in (C), colored by RCD pathway. **f** Ridge plots illustrating the UCell scores of apoptosis (top) and parthanatos (bottom) in each cell type, colored by age. **g** Boxplots showing the UCell scores of 13 RCD pathways in each major cell type. * $P<0.05$; ** $P<0.01$; *** $P<0.001$; **** $P<0.0001$; ns, not significant (two-tailed t-test)

including a reduction in follicles, an increase in stromal cells, and a reconfiguration of immune cell populations (Fig. 2i).

Changes in the transcriptional profiles of each cell type during murine ovarian aging

To investigate how genome-wide expression profiles of individual cell types change with age, we performed pairwise differential expression analyses between the 3-month group and each subsequent age group to identify the onset of DEGs accumulation. As shown in Fig. 3a, at 9 months, GCs and T&Ss showed the highest numbers of DEGs among all examined cell types at the same age, suggesting that GCs and T&Ss undergo early-onset molecular changes during ovarian aging. By 12 months, additional cell types including macrophages, monocytes, ECs, Epis and DCs, began to show significant perturbations. DEGs in Murs and NKs did not exhibit any increase until 15 months, while no DEGs were detected in BCs. Venn diagrams showed the intersections of DEGs identified in each comparative analysis. In cell types susceptible to aging, such as GCs and T&Ss, more than half of the DEGs identified in the 15-month versus 3-month comparison (OVA15M/OVA3M) were already detectable in the 9-month versus 3-month comparison (OVA9M/OVA3M). Conversely, in cell types such as DCs and NKs, the majority of transcriptional changes were observed around 15 months (Fig. 3b, Supplementary Table 2). These findings indicated markedly different accumulation trajectories of DEGs among ovarian cell types. Subsequently, we performed a KEGG enrichment analysis for the DEGs detected in OVA15M/OVA3M. Consistent with previous findings, several RCD pathways were enriched in different cell types, such as apoptosis in GCs, DCs, and macrophages, ferroptosis in T&Ss, and autophagy in monocytes and Epis (Fig. 3c). These results suggest that there may be distinct mechanisms driving the functional decline of different cell populations within the ovarian microenvironment during ovarian aging.

Transcriptomic signatures of multiple RCD patterns in various mouse ovarian cells

We then analyzed the RCD-related DEGs across various cell types, comparing the 3-month group with each subsequent age group (Fig. 4a). Consistent with previous findings, the 9-month and 12-month age groups demonstrated that T&Ss and GCs exhibited the highest number of RCD-related DEGs. In contrast, at 15 months, GCs and macrophages ranked as the top two subsets with the most RCD-related DEGs. Following this, the UCell algorithm was employed to evaluate the distribution of activity for each regulated pathway across different cell types within the comprehensive ovarian dataset (Fig. 4b). Notably, parthanatos showed the highest level of activity in GCs across all four age groups. In ECs, apoptosis was the predominant pathway active throughout the age groups. Lysosome-dependent cell death exhibited the highest activity in DCs, macrophages, and monocytes across all age groups. In contrast, the most active pathway in other cell types varied with age (Fig. 4c). These results suggested that multiple RCD pathways may be concurrently active within individual cells and the dominant RCD mode differed across cell types as well as reproductive stages.

Subsequently, we performed correlation analysis, revealing that the UCell score for apoptosis exhibited the highest correlation with age across all cell types (Fig. 4d). To ascertain the rate of change within various RCD pathways, we performed a quantitative analysis by calculating the slope of the linear regression model correlating the UCell scores of each pathway with age. Among these, parthanatos demonstrated the most rapid alteration with increasing age across a diverse range of cell types, encompassing GCs, T&Ss, ECs, Epis, Murs, macrophages, and NKs. Conversely, oxeiptosis was noted to undergo the most rapid changes with age in DCs and monocytes. Furthermore, in BCs, disulfidptosis was characterized by the highest absolute values of the UCell slope (Fig. 4e). The above findings emphasized the potential roles of apoptosis and parthanatos in ovarian aging. Apoptosis showed the strongest age association across many ovarian cell types, whereas parthanatos displayed a steeper age-associated increase in multiple cell populations. The ridge plot, as illustrated in Fig. 4f showed the UCell scores for apoptosis and parthanatos across all four age groups. In addition, a comparative analysis of the UCell scores of RCD pathways between the OVA3M and OVA15M groups revealed that the vast majority of pathways exhibited changes across a broad spectrum of cell types. However, certain RCD pathways, such as pyroptosis and netotic cell death, displayed notable cellular heterogeneity in their response (Fig. 4g). The differentiated response modes among cell types indicated a complex

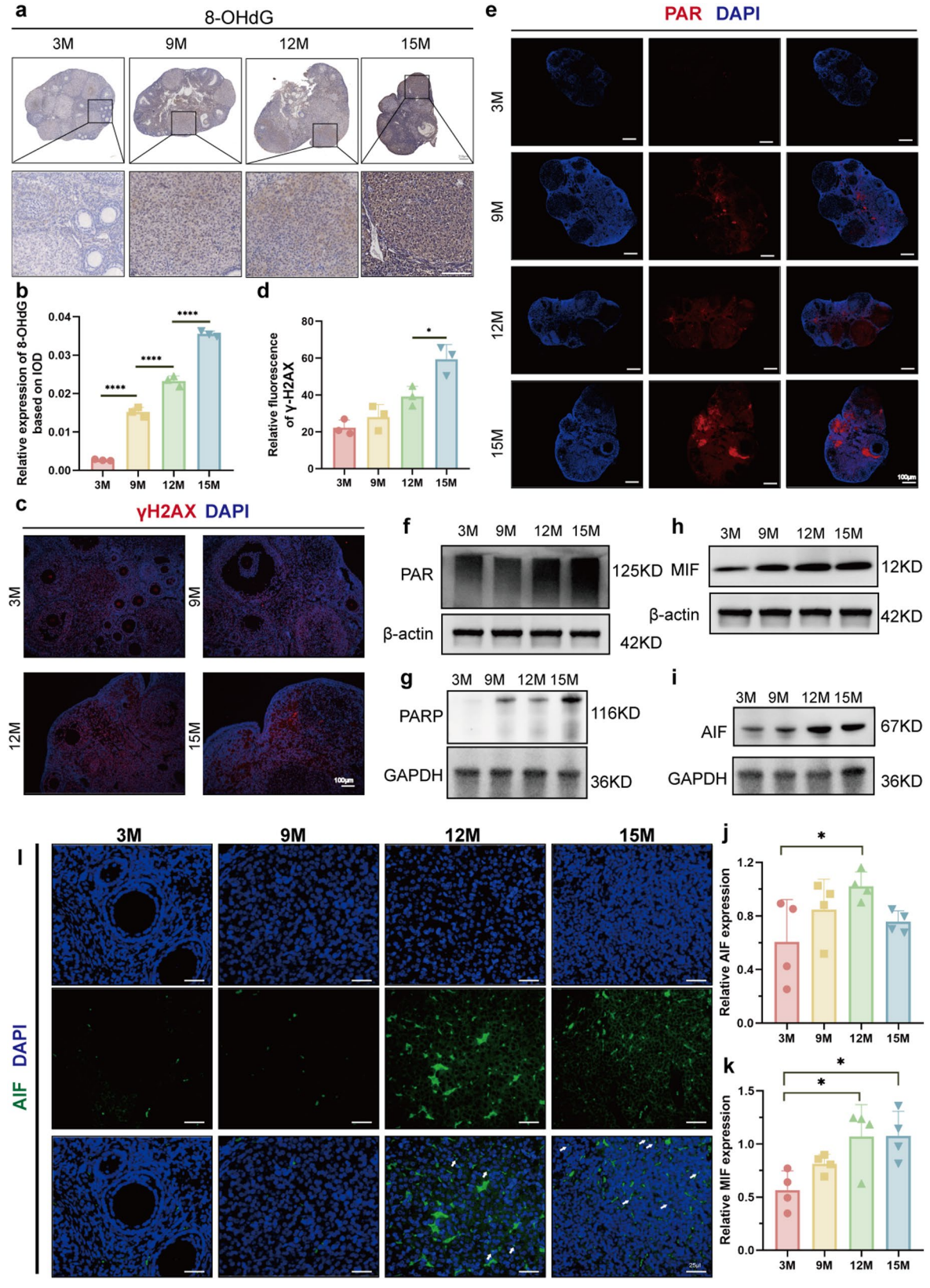

Fig. 5 (See legend on next page.)

(See figure on previous page.)

Fig. 5 Intensified DNA damage and parthanatos during ovarian aging. **a** Representative IHC images of 8-OHdG-stained ovarian sections from mice aged 3 M, 9 M, 12 M, and 15 M. Scale bars: 100 μm. **b** Statistical analysis on the staining intensity of 8-OHdG in ovaries from different age groups. **c** Representative IF images of γ-H2AX-stained. Scale bars: 100 μm **d** Statistical analysis on the fluorescence intensity of γ-H2AX in ovaries from different age groups. **e** Representative IF images of PAR-stained. Scale bars: 100 μm. **f-i** The expression levels of PAR, PARP, MIF, and AIF in ovaries from different age groups were detected via western blot. **j-k** Quantification of MIF and AIF protein levels was shown **l** The nuclear translocation of AIF was detected via IF. White arrows indicated the co-localization of DAPI and AIF. Scale bars: 25 μm. * $P < 0.05$; ** $P < 0.01$; *** $P < 0.001$; **** $P < 0.0001$, One-way ANOVA

interplay between various cell death pathways and the aging phenotypes.

Intensification of parthanatos during ovarian aging in murine models

The findings obtained from scRNA-seq prompted us to explore whether parthanatos, a regulated cell death pathway that has not received sufficient attention, becomes more pronounced in the ovary with advancing age, as indicated by the scRNA-seq data. Ovarian samples were collected from mice at 3, 9, 12 and 15 months of age. Initially, the expression levels of 8-OHdG and γH2AX, two well-established markers of DNA damage, were found to be significantly elevated in the ovaries as the mice aged. Notably, 8-OHdG positive staining was predominantly observed in corpora lutea, whereas γH2AX signals were detected in multiple ovarian compartments, including follicular granulosa cells, theca cells, and stromal regions (Fig. 5a-d). In response to this increased DNA damage, poly ADP-ribose polymerase (PARP) was activated, resulting in the accumulation of PAR, which was also enriched in corpora lutea and stromal areas (Fig. 5e-g). Additionally, the protein expression levels of macrophage migration inhibitory factor (MIF) and AIF showed an age-dependent increase (Fig. 5h-k). Immunofluorescence analysis revealed marked AIF nuclear translocation under aging conditions, most prominently in corpora lutea (Fig. 5l). Collectively, these data suggested that PARP1-dependent parthanatos is progressively activated during murine ovarian aging.

Uncovering the role of parthanatos in human ovarian aging via scRNA-seq

To explore the consistency and discordance of mechanisms underlying ovarian aging between mice and humans, the cohort GSE202601 containing single-nucleus sequencing (snRNA-seq) data of human ovarian tissues from 8 individuals aged 23 to 54 was employed (Fig. 6a). Through the Seurat standard process, 8 cell types were obtained: theca cells (TCs), smooth muscle cells (SMCs), stromal cells (SCs), lymphatic endothelial cells (LECs), immune cells (ICs), Granulosa cells (GCs), blood vascular endothelial cells (BECs), Epithelial cells (EpiCs) (Fig. 6b). Heatmap shows the top 5 marker genes of 8 types of cells (Fig. 6c). While cells from all the identified cell types were presented in every sample, the relative frequency of each cell type changed with age. The proportion of SCs and EpiCs showed an increasing trend in the old group; in contrast, GCs, BECs, LECs, and TCs declined with age. The proportions of SMCs and ICs were approximately steady between the two groups. The difference in cell proportion did not meet the significant criteria (Fig. 6d). These findings were comparable to those observed in mice, indicating a decrease in follicles and an increase in collagen deposition. Consistent with the murine ovary, GCs and SCs exhibited the highest number of DEGs between the younger and older groups, with counts of 1864 and 1593, respectively (Fig. 6e, Supplementary Table 3).

Subsequently, we calculated the UCell scores of each RCD pathway (Fig. 6f). Notably, ICs possessed the highest activity levels of seven pathways among the cell types, including apoptosis, ferroptosis, necroptosis, autophagy, PANoptosis, pyroptosis and lysosome-dependent death, suggesting an enhanced sensitivity to regulated cell death mechanisms of ICs, potentially central in ovarian immune surveillance and response. Given the ovary's pivotal endocrine role, a correlation analysis was conducted to investigate the association between the activities of 13 RCD pathways and expression levels of key genes for hormone synthesis (*STAR*, *CYP17A1*, *CYP11A1*, *CYP19A1*) (Fig. 6g). This analysis demonstrated the strongest inverse association with parthanatos, underscoring a potential inverse regulatory link between this cell death mechanism and the maintenance of ovarian hormonal balance. Additionally, the relationship between the activities of 13 RCD pathways and age across cell types was explored (Fig. 6h). Among the eight distinct cell types characterized within the human ovaries, parthanatos was found to exhibit the most robust positive correlation with age across five of these cell types: SCs, LECs, SMCs, GCs and ICs. This association suggested that parthanatos may play a pervasive and crucial role in age-related cellular function alterations within the ovary.

Corroborating parthanatos dysregulation in human ovarian aging using GTEx

Finally, we screened ovarian data in the GTEx V8 dataset and incorporated 22 samples in the 20–29 age group and 61 samples in the 50–59 age group (Fig. 7a). Morphological assessing showed similar changes between human and murine ovaries, that is, a distinct loss of healthy follicles and increase in corpus albicans and atretic follicles (Fig. 7b). A total of 859 DEGs were identified between

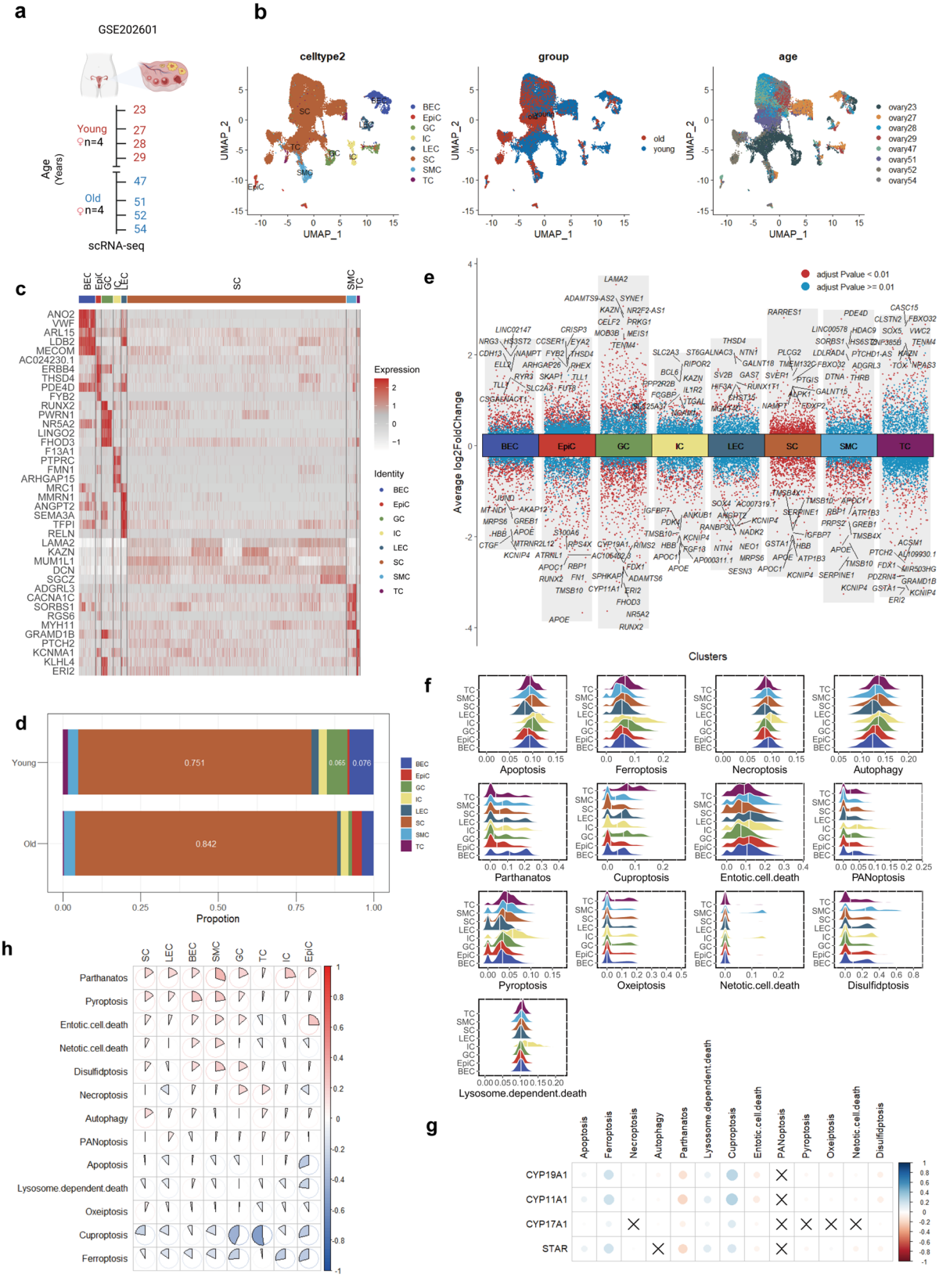

Fig. 6 (See legend on next page.)

(See figure on previous page.)

Fig. 6 Transcriptomic signature of multiple RCD pathways in various human ovarian cells using snRNA-seq dataset. **a** Cohort overview. Ovaries for snRNA sequencing were collected from females aged 23–54 years. **b** UMAP plot of ovarian cells, colored by cell type (left), group (middle), and age (right). **c** Heatmap showing the marker gene expression levels for each cell type in the human ovaries. **d** Stacked bar chart showing the proportion of major cell types in the young and old groups. **e** DEGs ($|\log_2 FC| > 0.25$, adjusted $P < 0.05$) in each major cell type between the old and young groups. The upregulated or downregulated genes that exhibited the highest 10 $\log_2 FC$ are labeled. **f** Ridge plot showing the UCell scores of 13 RCD pathways in each major cell type, colored by cell type. **g** Correlation analysis between the 13 RCD-related ssGSEA scores and steroidogenesis-related enzymes using all cells. **h** Correlation analysis between the 13 RCD-related ssGSEA scores and chronological age in each cell type

50 and 59 age group and 20–29 age group, among which 378 DEGs were upregulated and 481 DEGs were downregulated (Fig. 7c and Supplementary Table 4). Consistent with the results of mice, enrichment analysis for the upregulated DEGs revealed the involvement of immune-related pathways, such as "Immunoglobulin complex", "Antigen binding", while downregulated DEGs enriched in cell cycle, gamete generation, etc. (Fig. 7d).

To determine the RCD pathway activity for each sample, a ssGSEA analysis was carried out, indicating that the aged ovary had increased activity for parthanatos, entotic cell death, netotic cell death, apoptosis, ferroptosis, oxeiptosis, and PANoptosis, with only parthanatos reaching statistical significance. On the contrary, none of the pathways that showed a decrease in activity in the aged ovary reached statistical significance (Fig. 7e). Correlation analysis was conducted to explore the relationship between the activities of the 13 RCD pathways and the expression of key genes implicated in hormone synthesis, as previously discussed. The identification of pathways that exhibit negative correlation with these genes, including parthanatos, disulfidptosis, and netotic cell death, suggests a potential detrimental effect on ovarian function (Fig. 7f).

Considering the significantly increased activity of parthanatos and its inverse association with hormone synthesis genes during ovarian aging, gene modules correlated with the parthanatos phenotype were obtained by WGCNA analysis of 83 samples. Utilizing a soft threshold of 11, a minimum module size threshold of 30 genes, and a module merging criterion of similarity less than 0.25, we delineated a total of 10 non-gray modules (Fig. 7g). Notably, as shown in Fig. 7h, the 'MEblue' module was found to be closely related to the score of parthanatos within the non-gray module. Subsequently, univariate logistic regression analysis, with a significance threshold of $P < 0.05$, was performed to preliminarily identify 107 genes associated with patient age groups. Then LASSO regression analysis was conducted, which indicated that at an optimal gene inclusion count of 8, the model exhibited stable gene contraction and minimal partial likelihood deviance, with the optimal lambda value determined to be 0.0272 (Fig. 7i). Finally, an eight-gene signature was derived and used to formulate a risk score for ovarian aging, as delineated in the following equation (Fig. 7j): Risk score= (*CTC-444N24.6* * -0.119390818562094) + (*TRIM60P18* * -0.568983188887762) + (*MTMR9LP* * 0.70821444046537) + (*RP11-154H23.3* * -0.0927690121750645) + (*TCP10L* * 0.355810314174745) + (*ANKRD13B* * -1.08511369333606) + (*SEMA4F* * 1.38214725771393) + (*RP11-661O13.1* * -0.807505448694975). As shown in Fig. 7k, this parthanatos-related risk score was significantly higher in the old group, underscoring the potential clinical relevance of this gene signature in the context of ovarian aging.

Discussion

Human ovarian function is subject to a sharp decline at the age of late 20s, prominently featured in the decreased quantity and quality of oocytes [46]. Previous studies have revealed several pathogenic mechanisms for ovarian aging, such as cell death, oxidative damage [23], inflammation [47], cellular senescence [1], fibrosis [48] and mitochondrial dysfunction [49]. However, investigation into the specific cellular responses that occur during ovarian aging, such as regulated cell death, has just begun with the help of scRNA-seq or snRNA-seq. This knowledge will facilitate the development of targeted interventions for ovarian protection. In addition, due to ethical and tissue acquisition limitations, the mouse is the primary model in previous ovarian aging research. However, significant differences between rodents and humans cannot be overlooked, causing the necessity for a comprehensive comparison analysis. In this study, the clues from public bulk-seq data inspired us to create a single-cell dataset of aging mouse ovaries to investigate changes in cell composition, gene signatures, and potential biological processes. Especially, we have paid close attention to the activity change of 13 different types of RCD in ovaries across aging as well as the activity of various RCD types in 10 somatic cell types. Additionally, we also validated the activity change of these 13 RCD pathways in public data of human ovaries.

Nowadays, the advancement of scRNA-seq technology has elucidated the transcriptomic alterations occurring within each ovarian cell type throughout the aging process, facilitating the establishment of several single-cell atlases relevant to ovarian aging [23, 24, 50–53], with the murine rodents being the most frequently used model organisms. Nevertheless, the majority of existing atlases of ovarian aging predominantly featured mice from only the two distinct age groups of young and elderly, which may lead to the neglect of the nuanced and progressive

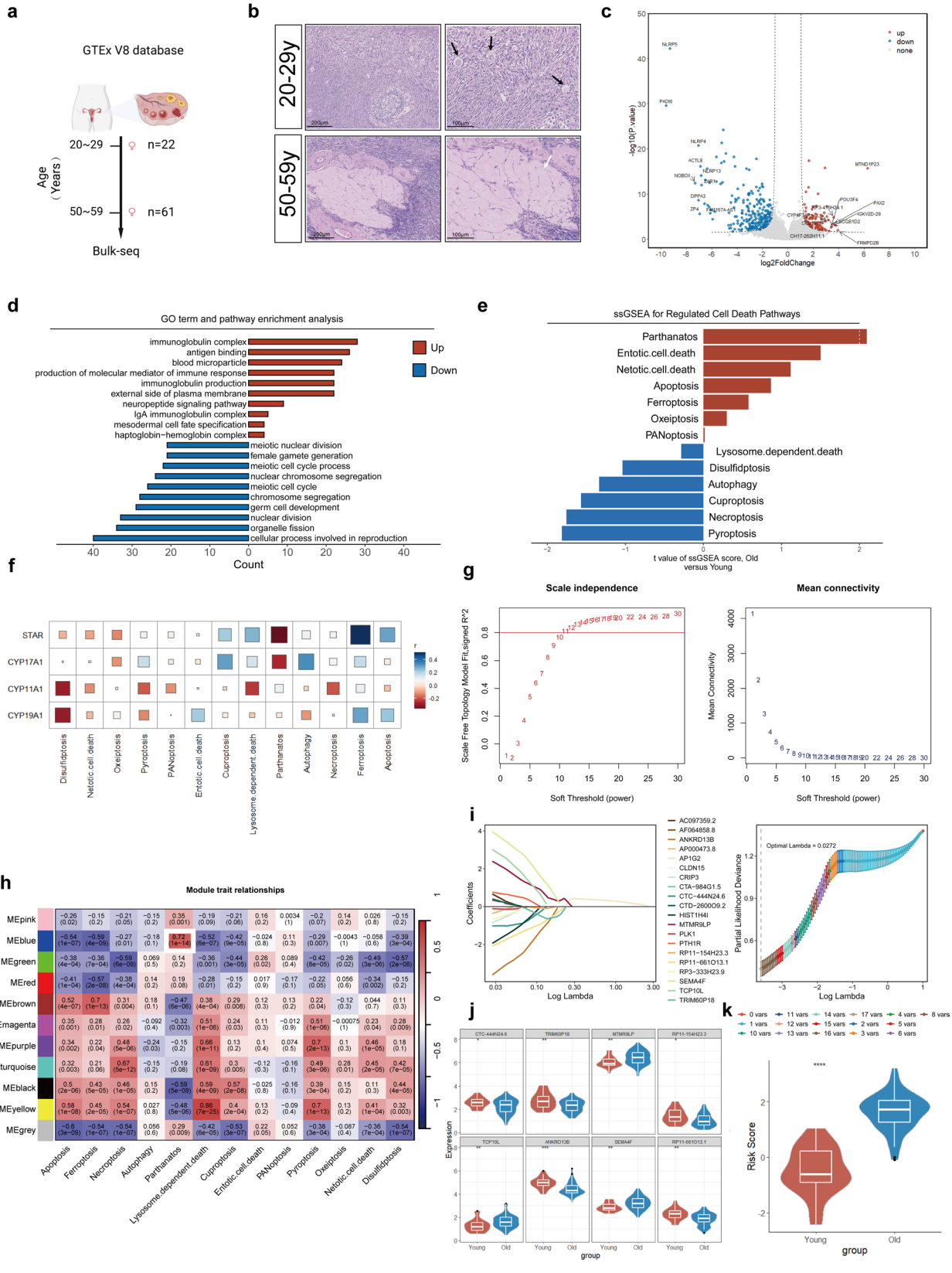

Fig. 7 (See legend on next page.)

(See figure on previous page.)

Fig. 7 Identification of the module closely related to parthanatos in ovarian aging by WGCNA. **a** Cohort overview. Transcriptome data of female ovarian tissues in the 20–29 age group and 50–59 age group were obtained from the GTEx V8 database. **b** H&E staining of human ovaries from each age group. Black arrows indicate follicles and white arrows indicate the corpus albicans. **c** Volcano plot showing 859 DEGs ($|\log_2 FC| > 0.25$, adjusted $P < 0.05$) between the 20–29 age group and 50–59 age group. The upregulated or downregulated genes that exhibited the highest 10 $\log_2 FC$ are labeled. **d** Representative GO terms and pathways enriched in upregulated and downregulated DEGs based on functional enrichment analysis. **e** ssGSEA analysis of 13 RCD pathways demonstrated by bar plots in 20–29 age and 50–59 age groups. The dotted lines indicate a *P*-value of 0.05. **f** Correlation analysis between the 13 RCD-related ssGSEA scores and steroidogenesis-related enzymes. **g** Scale-free exponent and average connectivity for each soft threshold. **h** Heatmap showing the correlations between module eigengenes and ssGSEA scores of 13 RCD pathways. **i** Distribution of LASSO coefficients for differential genes (left) and choice of the optimal lambda (right). **j** Violin plot showing the expression levels of the genes included in the model in each group. **k** Violin plot displaying the risk score distribution between the young and old groups. * $P < 0.05$; ** $P < 0.01$; *** $P < 0.001$; **** $P < 0.0001$; ns, not significant (two-tailed t-test)

dynamism inherent in the aging process. Hence, a multi-age-stage murine ovarian atlas was established in this study to provide more comprehensive information for the molecular and cellular dynamics across various stages of ovarian development and aging. The four age stages selected here respectively corresponded to the peak of reproductive capacity, the phase of accelerated decline in ovarian reserve yet still capable of reproduction, the stage approaching reproductive exhaustion, and the period of complete reproductive failure [54]. We noted that, despite the widely recognized rapid decline in ovarian function in mice occurring approximately at 8–9 months of age [53, 55], not all cell types within the ovary undergo significant alterations during this period. At 9 months, GCs and T&Ss cells exhibited the most pronounced changes in cell composition and gene expression profiles. Given their central roles in folliculogenesis and steroidogenesis, these compartments are among the most metabolically active in the ovary. Such functional demands may increase sensitivity to mitochondrial and oxidative stress and associated DNA-damage responses, which could contribute to earlier age-associated transcriptional changes [53]. In contrast, alterations in immune cells, particularly macrophages and monocytes, became prominent from 12 months onward. This may reflect a later phase of remodeling of the ovarian immune microenvironment. Such changes could be driven by accumulated tissue damage and stromal remodeling during advanced aging [56].

Parthanatos, discovered and defined in 2008, is mediated by the activation of PARP [57]. This leads to PAR polymers forming and moving to the cytosol and mitochondria, where they bind to AIF, triggering its release to the cytosol. AIF then pairs with MIF to form a complex that enters the nucleus, causing DNA fragmentation and chromatin condensation [58, 59]. Parthanatos is involved in many diseases, such as brain disorders like Parkinson's disease and Alzheimer's disease [59, 60], colitis [61], stroke [62], and leukemia [63]. Using cumulus GCs from DOR patients and normal ovarian reserve patients, Batnasan et al. demonstrated that PAR expression and AIF nuclear translocation were significantly higher in cumulus GCs of DOR patients, which suggests an association between parthanatos and DOR pathophysiology [22]. In our study, parthanatos demonstrated the steepest gradient of UCell in seven of the ten murine ovarian cell types examined, indicating a sharp change in its activity occurred with advancing age. Partial overlap among curated gene sets arising from biological crosstalk and uneven annotation depth across RCD pathways may introduce redundancy [18]. To address this, we quantified gene set overlap and conducted a parthanatos-specific sensitivity analysis using a score restricted to parthanatos-unique genes; the strong correlation with the original score and the preserved age-associated trend support the robustness of our main conclusions. In addition, our in vivo animal experiments further confirmed that the initiation of parthanatos was a consequence of progressively severe oxidative damage in ovarian cells. Although definitive cell-type assignment will require future co-localization with cell-type markers or spatially resolved approaches, our experimental results preliminarily support an age-associated increase in parthanatos-related signals in the ovary as a whole. As for humans, at the single-cell level, the activity of parthanatos showed the highest positive correlation with chronological age across most cell types, and conversely, a negative correlation with the gene expression profiles associated with hormone synthesis. In addition, according to data from the GTEx V8 dataset, only the activity increase of the parthanatos pathway reached statistical significance between the young and old groups. Therefore, precise modulation of parthanatos to influence ovarian aging deserves further investigation in future studies. It is worth mentioning that previous studies have demonstrated that senescent cells always upregulated the senescence-associated anti-apoptotic pathways (SCAPs) to protect themselves from the proapoptotic microenvironment [64–66]. However, the removal of senescent cells becomes essential once the detrimental chemicals produced by senescent cells are released to the microenvironment and cause damage to normal cells. Therefore, the upregulation of these RCD pathways in the ovary may reflect the competition between cellular senescence and cell death in the process of ovarian aging. The factors determining cell fate at this juncture warrant further investigation.

In this study, we compared the reproductive cell atlas as well as the changes in RCD activities between humans and mice. Similarities between mouse and human ovaries in terms of cellular composition and age-related transcriptomic changes were revealed, indicating that the mouse model may effectively mirror the essential biological features of human ovarian aging. Nevertheless, notable interspecies differences still existed in specific genes or regulatory pathways. For instance, the human ovary demonstrates greater stability in RCD activity compared to that of mice, with only the parthanatos activity exhibiting a statistically significant difference. This suggests a superior capacity in humans to maintain ovarian physiological homeostasis. Consequently, when extrapolating findings from murine models to clinical applications, it is essential to carefully consider these interspecies differences and to conduct more in-depth cross-species comparative analyses and verifications.

This study identified the potential role of certain RCD modes in ovarian aging using single-cell sequencing data and transcriptome sequencing data, serving as a compass for future research. However, since some key processes of initiation and amplification of RCD were regulated at the level of RNA translation or posttranslational modifications [9], confirmation of their exact roles in ovarian aging requires more experimental verification. In addition, no additional clinical information related to the samples is available in the public human ovarian dataset, which hinders us from further investigating the correlation between the RCD and clinical characteristics like the serum sex hormone levels and antral follicle count. Especially, in the GTEx v8 data used here, the open access release provides only limited donor metadata (Sex, 10-year age bracket, and Hardy scale). More detailed information that may affect ovarian function, such as exact age, BMI, comorbidities, hormone use, and cause of death, is unavailable without an approved dbGaP application. Consequently, this hindered us from adjusting our analyses for these covariates. Future validation in independent cohorts with richer clinical characteristics will be required. Moreover, since the diameter of an oocyte is always larger than the technical limitations of scRNA-seq (i.e., cells should be < 40 μm in diameter) and their number is notably fewer than the somatic cells in the ovary, both the mouse ovarian single-cell atlas we created and the human ovarian scRNA-seq data available online failed to capture sufficient oocytes for further analysis. Thus, it would be promising to investigate the role of each RCD pathway in oocyte death with advanced technologies, which can help develop fertility-protective strategies targeting key pathways.

Conclusions

In summary, this study developed an atlas of aging murine ovaries, explored the patterns of 13 RCD pathways, and conducted comparative analyses with human data using publicly available datasets. The findings suggest that multiple RCD patterns may interactively influence ovarian aging, with each pathway contributing to varying extents across distinct cell types. Notably, parthanatos emerges as a common RCD for ovarian aging in both mice and humans. The study offers valuable insights into the diverse mechanisms of cell death in ovarian aging, potentially informing the development of therapeutic targets for fertility preservation strategies.

Supplementary Information

The online version contains supplementary material available at https://doi.org/10.1186/s13048-026-02024-x.

Supplementary Material 1.

Supplementary Material 2.

Supplementary Material 3.

Supplementary Material 4.

Supplementary Material 5.

Supplementary Material 6.

Supplementary Material 7.

Supplementary Material 8.

Acknowledgements

Thanks to the Singleron Biotechnologies Company for performing bioinformatics analysis.

Authors' contributions

J.Z., M.L. and S.W. conceived, designed and supervised the research. Q.Z., Y.Z. and M.L. performed animal experiments and bioinformatics analysis of the scRNA-seq data. Q.Z., G.C., T.W., S.W. and J.Z. wrote, reviewed, and edited the manuscript. All authors discussed the results and approved the final manuscript.

Funding

This work was supported by the grants from the National Natural Science Foundation of China (NO. 82371648; No. 82471678), and the Natural Science Foundation of Hubei Province General Program Project (2025AFB489) and Interdisciplinary Research Program of HUST (2025JCYJ034).

Data availability

The datasets supporting the conclusions of this article are available in the National Center for Biotechnology Information (NCBI) Gene Expression Omnibus (GEO) under the accession code 'GSE241318'.

Declarations

Ethics approval and consent to participate

All animal care and procedures abided by ARRIVE guidelines and were conducted per the guidelines approved by the Institutional Animal Care and Use Committee of Huazhong University of Science and Technology (TJH-202103015).

This study utilized paraffin-embedded human ovarian sections obtained from the Department of Pathology at Tongji Hospital. Written informed consent

was obtained from all participants in the study. All experimental procedures involving human tissues were conducted in accordance with the guidelines of and approved by the Ethics Committee of Huazhong University of Science and Technology (TJ-IRB20210319).
The study adhered to the ethical principles outlined in the Declaration of Helsinki.

Consent for publication
Not applicable.

Competing interests
The authors declare no competing interests.

Received: 15 October 2025 / Accepted: 8 February 2026
Published online: 13 February 2026

References

1. Lu H, Jing Y, Zhang C, Ma S, Zhang W, Huang D, et al. Aging hallmarks of the primate ovary revealed by spatiotemporal transcriptomics. Protein Cell. 2024;15(5):364–84. https://doi.org/10.1093/procel/pwad063.
2. Tilly JL, Sinclair DA. Germline energetics, aging, and female infertility. Cell Metab. 2013;17(6):838–50.
3. Ashapkin V, Suvorov A, Pilsner JR, Krawetz SA, Sergeyev O. Age-associated epigenetic changes in mammalian sperm: implications for offspring health and development. Hum Reprod Update. 2023;29(1):24–44.
4. Levine ME, Lu AT, Chen BH, Hernandez DG, Singleton AB, Ferrucci L, et al. Menopause accelerates biological aging. Proc Natl Acad Sci U S A. 2016;113(33):9327–32.
5. Nappi RE, Chedraui P, Lambrinoudaki I, Simoncini T. Menopause: a cardiometabolic transition. Lancet Diabetes Endocrinol. 2022;10(6):442–56.
6. Cheng G, Wang M, Sun H, Lai J, Feng Y, Liu H, et al. Age at menopause is inversely related to the prevalence of common gynecologic cancers: a study based on NHANES. Front Endocrinol (Lausanne). 2023;14:1218045.
7. Sochocka M, Karska J, Pszczołowska M, Ochnik M, Fułek M, Fułek K, et al. Cognitive decline in early and premature menopause. Int J Mol Sci. 2023;24(7):6566. https://doi.org/10.3390/ijms24076566.
8. Xu Z, Chung H-F, Dobson AJ, Wilson LF, Hickey M, Mishra GD. Menopause, hysterectomy, menopausal hormone therapy and cause-specific mortality: cohort study of UK biobank participants. Hum Reprod. 2022;37(9):2175–85.
9. Tang D, Kang R, Berghe TV, Vandenabeele P, Kroemer G. The molecular machinery of regulated cell death. Cell Res. 2019;29(5):347–64.
10. Wang H, Wang X, Huang L, Wang C, Yu F, Ye L. Overburdened ferroptotic stress impairs tooth morphogenesis. Elife. 2023;12:RP88745. https://doi.org/10.7554/eLife.88745.
11. Habiba M, Heyn R, Bianchi P, Brosens I, Benagiano G. The development of the human uterus: morphogenesis to menarche. Hum Reprod Update. 2021;27(1):1–26. https://doi.org/10.1093/humupd/dmaa036.
12. Moriishi T, Kawai Y, Fukuyama R, et al. Bcl2l1 deficiency in osteoblasts reduces the trabecular bone dueto enhanced osteoclastogenesis likely through osteoblast apoptosis. Int J Mol Sci. 2023;24(24):17319. https://doi.org/10.3390/ijms242417319.
13. Yuan G, Ning L, Qing X, Lujia W, Kai H, Xiangyang X, et al. BFGF attenuates aortic valvular interstitial cell calcification by inhibiting Endoplasmic reticulum stress-mediated apoptosis. Exp Cell Res. 2024;434(2):113889.
14. Jing Z, Li Y, Zhang H, Chen T, Yu J, Xu X, et al. Tobacco toxins induce osteoporosis through ferroptosis. Redox Biol. 2023;67:102922.
15. Santagostino SF, Assenmacher C-A, Tarrant JC, Adedeji AO, Radaelli E. Mechanisms of regulated cell death: current perspectives. Vet Pathol. 2021;58(4):596–623.
16. Liu X, Nie L, Zhang Y, Yan Y, Wang C, Colic M, et al. Actin cytoskeleton vulnerability to disulfide stress mediates Disulfidptosis. Nat Cell Biol. 2023;25(3):404–14.
17. Sun X, Yang Y, Meng X, Li J, Liu X, Liu H. PANoptosis: Mechanisms, biology, and role in disease. Immunol Rev. 2024;321(1):246–62.
18. Bertheloot D, Latz E, Franklin BS. Necroptosis, pyroptosis and apoptosis: an intricate game of cell death. Cell Mol Immunol. 2021;18(5):1106–21.
19. Stringer JM, Alesi LR, Winship AL, Hutt KJ. Beyond apoptosis: evidence of other regulated cell death pathways in the ovary throughout development and life. Hum Reprod Update. 2023;29(4):434–56.
20. Yadav PK, Tiwari M, Gupta A, Sharma A, Prasad S, Pandey AN, et al. Germ cell depletion from mammalian ovary: possible involvement of apoptosis and autophagy. J Biomed Sci. 2018;25(1):36.
21. Lliberos C, Liew SH, Mansell A, Hutt KJ. The inflammasome contributes to depletion of the ovarian reserve during aging in mice. Front Cell Dev Biol. 2020;8:628473.
22. Batnasan E, Xie S, Zhang Q, Li Y. Observation of parthanatos involvement in diminished ovarian reserve patients and melatonin's protective function through inhibiting ADP-Ribose (PAR) expression and preventing AIF translocation into the nucleus. Reprod Sci. 2020;27(1):75–86.
23. Wang S, Zheng Y, Li J, Yu Y, Zhang W, Song M, et al. Single-cell transcriptomic atlas primate ovarian aging cell. 2020;180(3):585–600.e19. https://doi.org/10.1016/j.cell.2020.01.009.
24. Zhou C, Guo Q, Lin J, Wang M, Zeng Z, Li Y, et al. Single-Cell atlas of human ovaries reveals the role of the pyroptotic macrophage in ovarian aging. Adv Sci (Weinh). 2024;11(4):e2305175.
25. Cai M, Li Q, Cao Y, Huang Y, Yao H, Zhao C, et al. Quercetin activates autophagy to protect rats ovarian granulosa cells from H2O2-induced aging and injury. Eur J Pharmacol. 2024;966:176339.
26. Li P, Dou Q, Zhang D, Xiang Y, Tan L. Melatonin regulates autophagy in granulosa cells from patients with premature ovarian insufficiency via activating Foxo3a. Aging. 2024;16(1):844–56.
27. Niu C, Jiang D, Guo Y, Wang Z, Sun Q, Wang X, et al. Spermidine suppresses oxidative stress and ferroptosis by Nrf2/HO-1/GPX4 and Akt/FHC/ACSL4 pathway to alleviate ovarian damage. Life Sci. 2023;332:122109.
28. Winkler I, Tolkachov A, Lammers F, et al. The cycling and aging mouse female reproductive tract at single-cell resolution. Cell. 2024;187(4):981–98.e25. https://doi.org/10.1016/j.cell.2024.01.021.
29. Goldman JM, Murr AS, Cooper RL. The rodent estrous cycle: characterization of vaginal cytology and its utility in toxicological studies. Birth Defects Res B Dev Reprod Toxicol. 2007;80(2):84–97.
30. Ma S, Sun S, Geng L, et al. Caloric restriction reprograms the single-cell transcriptional landscape of rattus norvegicus aging. Cell. 2020;180(5):984–1001.e22. https://doi.org/10.1016/j.cell.2020.02.008.
31. Dura B, Choi J-Y, Zhang K, Damsky W, Thakral D, Bosenberg M, et al. scFTD-seq: freeze-thaw Lysis based, portable approach toward highly distributed single-cell 3' mRNA profiling. Nucleic Acids Res. 2019;47(3):e16.
32. Korsunsky I, Millard N, Fan J, Slowikowski K, Zhang F, Wei K, et al. Fast, sensitive and accurate integration of single-cell data with harmony. Nat Methods. 2019;16(12):1289–96. https://doi.org/10.1038/s41592-019-0619-0.
33. Jin C, Wang X, Yang J, Kim S, Hudgins AD, Gamliel A, et al. Molecular and genetic insights into human ovarian aging from single-nuclei multi-omics analyses. Nat Aging. 2025;5(2):275–90. https://doi.org/10.1038/s43587-024-00762-5.
34. Ansere VA, Ali-Mondal S, Sathiaseelan R, Garcia DN, Isola JVV, Henseb JD, et al. Cellular hallmarks of aging emerge in the ovary prior to primordial follicle depletion. Mech Ageing Dev. 2021;194:111425.
35. Love MI, Huber W, Anders S. Moderated Estimation of fold change and dispersion for RNA-seq data with DESeq2. Genome Biol. 2014;15(12):550.
36. Wu T, Hu E, Xu S, Chen M, Guo P, Dai Z, et al. ClusterProfiler 4.0: A universal enrichment tool for interpreting omics data. Innov (Camb). 2021;2(3):100141.
37. Zou Y, Xie J, Zheng S, Liu W, Tang Y, Tian W, et al. Leveraging diverse cell-death patterns to predict the prognosis and drug sensitivity of triple-negative breast cancer patients after surgery. Int J Surg. 2022;107:106936.
38. Hänzelmann S, Castelo R, Guinney J. GSVA: gene set variation analysis for microarray and RNA-seq data. BMC Bioinformatics. 2013;14:7.
39. Ritchie ME, Phipson B, Wu D, Hu Y, Law CW, Shi W, et al. Limma powers differential expression analyses for RNA-sequencing and microarray studies. Nucleic Acids Res. 2015;43(7):e47.
40. Andreatta M, Carmona SJ, UCell. Robust and scalable single-cell gene signature scoring. Comput Struct Biotechnol J. 2021;19:3796–8.
41. Lenth RV. Least-Squares means: the R package Lsmeans. J Stat Softw. 2016;69(1):1–33.
42. Langfelder P, Horvath S. WGCNA: an R package for weighted correlation network analysis. BMC Bioinformatics. 2008;9:559.
43. Tibshirani R. Regression shrinkage and selection via the Lasso. J Roy Stat Soc: Ser B (Methodol). 2018;58(1):267–88.
44. Russ JE, Haywood ME, Lane SL, Schoolcraft WB, Katz-Jaffe MG. Spatially resolved transcriptomic profiling of ovarian aging in mice. iScience. 2022;25(8):104819.

45. Umehara T, Winstanley YE, Andreas E, Morimoto A, Williams EJ, Smith KM, et al. Female reproductive life span is extended by targeted removal of fibrotic collagen from the mouse ovary. Sci Adv. 2022;8(24):eabn4564.
46. Chiang JL, Shukla P, Pagidas K, Ahmed NS, Karri S, Gunn DD, et al. Mitochondria in ovarian aging and reproductive longevity. Ageing Res Rev. 2020;63:101168.
47. Orisaka M, Mizutani T, Miyazaki Y, Shirafuji A, Tamamura C, Fujita M, et al. Chronic low-grade inflammation and ovarian dysfunction in women with polycystic ovarian syndrome, endometriosis, and aging. Front Endocrinol (Lausanne). 2023;14:1324429.
48. Landry DA, Yakubovich E, Cook DP, Fasih S, Upham J, Vanderhyden BC. Metformin prevents age-associated ovarian fibrosis by modulating the immune landscape in female mice. Sci Adv. 2022;8(35):eabq1475.
49. May-Panloup P, Boucret L, Chao de la Barca J-M, Desquiret-Dumas V, Ferré-L'Hotellier V, Morinière C, et al. Ovarian ageing: the role of mitochondria in oocytes and follicles. Hum Reprod Update. 2016;22(6):725–43.
50. Yang Q, Chen W, Cong L, Wang M, Li H, Wang H, et al. NADase CD38 is a key determinant of ovarian aging. Nat Aging. 2024;4(1):110–28.
51. Wu M, Tang W, Chen Y, Xue L, Dai J, Li Y, et al. Spatiotemporal transcriptomic changes of human ovarian aging and the regulatory role of FOXP1. Nat Aging. 2024;4(4):527–45.
52. Winkler I, Tolkachov A, Lammers F, Lacour P, Daugelaite K, Schneider N, et al. The cycling and aging mouse female reproductive tract at single-cell resolution. Cell. 2024;187(4):981–e9825.
53. Isola JVV, Ocañas SR, Hubbart CR, Ko S, Mondal SA, Hense JD, et al. A single-cell atlas of the aging mouse ovary. Nat Aging. 2024;4(1):145–62.
54. Franks LM, Payne J. The influence of age on reproductive capacity in C57BL mice. J Reprod Fertil. 1970;21(3):563–5.
55. Diaz Brinton R. Minireview: translational animal models of human menopause: challenges and emerging opportunities. Endocrinology. 2012;153(8):3571–8.
56. Ben Yaakov T, Wasserman T, Aknin E, Savir Y. Single-cell analysis of the aged ovarian immune system reveals a shift towards adaptive immunity and attenuated cell function. Elife. 2023;12:e74915. https://doi.org/10.7554/eLife.74915.
57. Andrabi SA, Dawson TM, Dawson VL. Mitochondrial and nuclear cross talk in cell death: parthanatos. Ann N Y Acad Sci. 2008;1147:233–41.
58. Park W, Wei S, Kim B-S, Kim B, Bae S-J, Chae YC, et al. Diversity and complexity of cell death: a historical review. Exp Mol Med. 2023;55(8):1573–94.
59. Liu L, Li J, Ke Y, Zeng X, Gao J, Ba X, et al. The key players of parthanatos: opportunities for targeting multiple levels in the therapy of parthanatos-based pathogenesis. Cell Mol Life Sci. 2022;79(1):60.
60. Lee MH, Um K-H, Lee SW, Sun YJ, Gu D-H, Jo YO, et al. Bi-directional regulation of AIMP2 and its splice variant on PARP-1-dependent neuronal cell death; therapeutic implication for parkinson's disease. Acta Neuropathol Commun. 2024;12(1):5.
61. Zhu L, Xie Z, Yang G, Zhou G, Li L, Zhang S. Stanniocalcin-1 promotes PARP1-Dependent cell death via JNK activation in colitis. Adv Sci (Weinh). 2024;11(5):e2304123.
62. Wang L, Ye B, Liu Y, Li J, Li C, Wen M, et al. Xuebijing injection attenuates heat Stroke-Induced brain injury through oxidative stress blockage and parthanatos modulation via PARP-1/AIF signaling. ACS Omega. 2023;8(37):33392–402.
63. Maru B, Messikommer A, Huang L, Seipel K, Kovecses O, Valk PJM, et al. PARP-1 improves leukemia outcomes by inducing parthanatos during chemotherapy. Cell Rep Med. 2023;4(9):101191.
64. Zhu Y, Tchkonia T, Pirtskhalava T, Gower AC, Ding H, Giorgadze N, et al. The achilles' heel of senescent cells: from transcriptome to senolytic drugs. Aging Cell. 2015;14(4):644–58.
65. Xu M, Pirtskhalava T, Farr JN, Weigand BM, Palmer AK, Weivoda MM, et al. Senolytics improve physical function and increase lifespan in old age. Nat Med. 2018;24(8):1246–56.
66. Garcia-Arias JM, Pinal N, Cristobal-Vargas S, Estella C, Morata G. Lack of apoptosis leads to cellular senescence and tumorigenesis in drosophila epithelial cells. Cell Death Discov. 2023;9(1):281.

Publisher's note